ARMY RESEARCH LABORATORY

Explosive Residue Detection by Laser Surface Photo-fragmentation–Fragment Detection Spectroscopy: II. *In Situ* and Real-time Monitoring of RDX, HMX, CL20, and TNT, by an Improved Ion Probe

by Jerry B. Cabalo and Rosario C. Sausa

ARL-TR-3478 **April 2005**

NOTICES

Disclaimers

The findings in this report are not to be construed as an official Department of the Army position unless so designated by other authorized documents.

Citation of manufacturer's or trade names does not constitute an official endorsement or approval of the use thereof.

DESTRUCTION NOTICE—Destroy this report when it is no longer needed. Do not return it to the originator.

Army Research Laboratory
Aberdeen Proving Ground, MD 21005-5069

ARL-TR-3478 **April 2005**

Explosive Residue Detection by Laser Surface Photo-fragmentation–Fragment Detection Spectroscopy: II. *In Situ* and Real-time Monitoring of RDX, HMX, CL20, and TNT, by an Improved Ion Probe

Jerry B. Cabalo and Rosario C. Sausa
Weapons and Materials Research Directorate, ARL

REPORT DOCUMENTATION PAGE

Form Approved
OMB No. 0704-0188

1. REPORT DATE *(DD-MM-YYYY)*	2. REPORT TYPE	3. DATES COVERED (From - To)
April 2005	Final	October 2002 to June 2004

4. TITLE AND SUBTITLE

Explosive Residue Detection by Laser Surface Photo-fragmentation–Fragment Detection Spectroscopy: II. *In Situ* and Real-time Monitoring of RDX, HMX, CL20, and TNT, by an Improved Ion Probe

5a. CONTRACT NUMBER

5b. GRANT NUMBER

5c. PROGRAM ELEMENT NUMBER

6. AUTHOR(S)

Jerry B. Cabalo and Rosario C. Sausa (both of ARL)

5d. PROJECT NUMBER
622618H8011

5e. TASK NUMBER

5f. WORK UNIT NUMBER

7. PERFORMING ORGANIZATION NAME(S) AND ADDRESS(ES)

U.S. Army Research Laboratory
Weapons and Materials Research Directorate
Aberdeen Proving Ground, MD 21005-5069

8. PERFORMING ORGANIZATION REPORT NUMBER

ARL-TR-3478

9. SPONSORING/MONITORING AGENCY NAME(S) AND ADDRESS(ES)

10. SPONSOR/MONITOR'S ACRONYM(S)

11. SPONSOR/MONITOR'S REPORT NUMBER(S)

12. DISTRIBUTION/AVAILABILITY STATEMENT

Approved for public release; distribution is unlimited.

13. SUPPLEMENTARY NOTES

14. ABSTRACT

We measured trace concentrations of hexahydro-1,3,5-hexanitro-1,3,5-triazine [RDX], octohydro-1,3,5,7-octonitro-1,3,5,7-octazocine [HMX], hexanitrohexazaisowurtzitane [CL20], and 2,4,6-trinitrotoluene [TNT] by surface laser photo-fragmentation-fragment detection (SPF-FD) spectroscopy at ambient temperature and pressure. In this technique, a low power, 248-nm laser photo-fragments the target molecule on the surface of a substrate, and a low power, 226-nm laser ionizes the resulting nitricoxide (NO) fragment by resonance-enhanced multi-photon ionization by means of its A-X (0,0) transitions near 226 nm. Two different probes collect the ions: one with miniature, square electrodes mounted vertical to the substrate and the other with similar electrodes mounted horizontal to the substrate. The horizontal electrodes contain 2-mm holes for laser beam passage. We tested both probes on the selected explosives and modeled their electric field in the presence of a substrate with an ion optics simulation program. Our results show that the horizontal probe is about ten times more sensitive than the vertical probe because its electric field is perturbed by the substrate to a lesser extent than is the electric field of the vertical probe. The limits of detection of the various explosives range from 1 to 15 ng/cm^2 (S/N=3) at 1 atm and room temperature and depend mostly on the mechanism for NO formation. NO is formed with a room-temperature, Boltzmann, rotational-vibrational, population distribution. We also present an ultraviolet absorption spectrum of CL20 and report its extinction coefficient at 248 nm.

15. SUBJECT TERMS

explosive detection; laser surface photo-fragmentation–fragment detection spectroscopy; resonance-enhanced ionization; RDX

16. SECURITY CLASSIFICATION OF:			17. LIMITATION OF ABSTRACT	18. NUMBER OF PAGES	19a. NAME OF RESPONSIBLE PERSON
a. REPORT	b. ABSTRACT	c. THIS PAGE	SAR	30	Jerry B. Cabalo
Unclassified	Unclassified	Unclassified			19b. TELEPHONE NUMBER (*Include area code*) 410-306-0660

Standard Form 298 (Rev. 8/98)
Prescribed by ANSI Std. Z39.18

Contents

List of Figures

List of Tables

Acknowledgments

We thank the following people for their contributions:

- Dr. Betsy Rice of the U.S. Army Research Laboratory (ARL) for calculating the N-NO2 bond energy in CL20,
- Drs. Rose Pesce-Rodriguez and Pamela Kaste of ARL for the energetic material samples, and
- Drs. Anthony Kotlar and Michael Schroeder of ARL for many helpful discussions.

We also thank the National Research Council and the ARL Director's Research Initiative for support.

INTENTIONALLY LEFT BLANK

1. Introduction

The sensitive detection of explosive compounds in real time at ambient pressure and temperature is a key issue for law enforcement and airport security. Two laser spectroscopic techniques for detecting 2,4,6 trinitrotoluene [TNT] in the gas phase are cavity ring-down spectroscopy (CRDS) (*1*, *2*) and laser photo-fragmentation-fragment detection (PF-FD) spectroscopy (*3* through *7*). The CRDS technique probes the parent molecule, whereas the PF-FD technique probes the characteristic nitricoxide (NO) photo-fragment by laser-induced fluorescence (LIF) (*3* through *7*) or resonance-enhanced multiphoton ionization (REMPI) (*7*). The NO fragment is characteristic of the nitrogen dioxide (NO_2) functional group that is present in these molecules. Both techniques can detect TNT in the parts-per-million/volume (ppm/v) to parts-per-billion/volume (ppb/v) range near ambient conditions. However, these techniques cannot detect other important energetic materials such as hexahydro-1,3,5-hexanitro-1,3,5-triazine [RDX], octohydro-1,3,5,7-octonitro-1,3,5,7-octazocine [HMX], or hexanitrohexazaisowurtzitane [CL20] at ambient conditions because their vapor pressure concentrations are several of magnitudes less than the vapor pressure concentration of TNT at 298 K and 1 atmosphere (atm) (*8* through *11*). Structures of the energetic materials are shown in figure 1.

Laser irradiation of the solid energetic materials with ultraviolet (UV) light is a means of generating gaseous molecules or fragments that can be detected by mass spectrometry, optical spectroscopy, or both. Photothermal and photochemical processes produce atomic and molecular fragments from the surface. Tang and coworkers show that the 226-nm irradiation of RDX produces positive and negative ion masses ranging from 15 to 176 atomic mass units (a.m.u.) (*12*). They assign the mass:charge (m:z) = 30 peak to NO. Dickinson and coworkers observed small masses of neutral and ionic species, including NO, as well as photoelectrons, when they irradiated RDX crystals with 248-nm light at a fluence < 5 mJ/cm^2 (*13*). As they increased the laser fluence, they observed an increase in the kinetic energy of the products. They observed a clear etching of the crystal at a laser fluence ≥ 90 mJ/cm^2 and an intense peak attributable to NO. NO is formed in its long-lived, metastable, electronic state ($\tau \sim 50\ \mu s$) from the collisional re-neutralization of energetic NO^+. At a laser fluence of ~600mJ/cm^2, they observed a chemi-luminescence at 385 nm from electronically excited cyanogen (CN).

Our recent work on RDX sensing shows that the surface PF-FD (SPF-FD) technique can detect RDX residues *in situ* and in real time at ambient conditions (*14*). In this technique, a low power laser operating in the UV region photo-fragments RDX on a surface, and a second low power laser tuned to 226 nm ionizes the characteristic NO fragment by REMPI using its A-X (0,0) transitions. An ion probe with miniature, square electrodes collects the resulting electrons and ions. We observe that exciting RDX at 248 nm yields a greater ion signal than exciting it at 266 or 308 nm. The detection limit is ~14 ng/cm^2 (signal to noise [S/N] = 3) at 248 nm and ambient conditions.

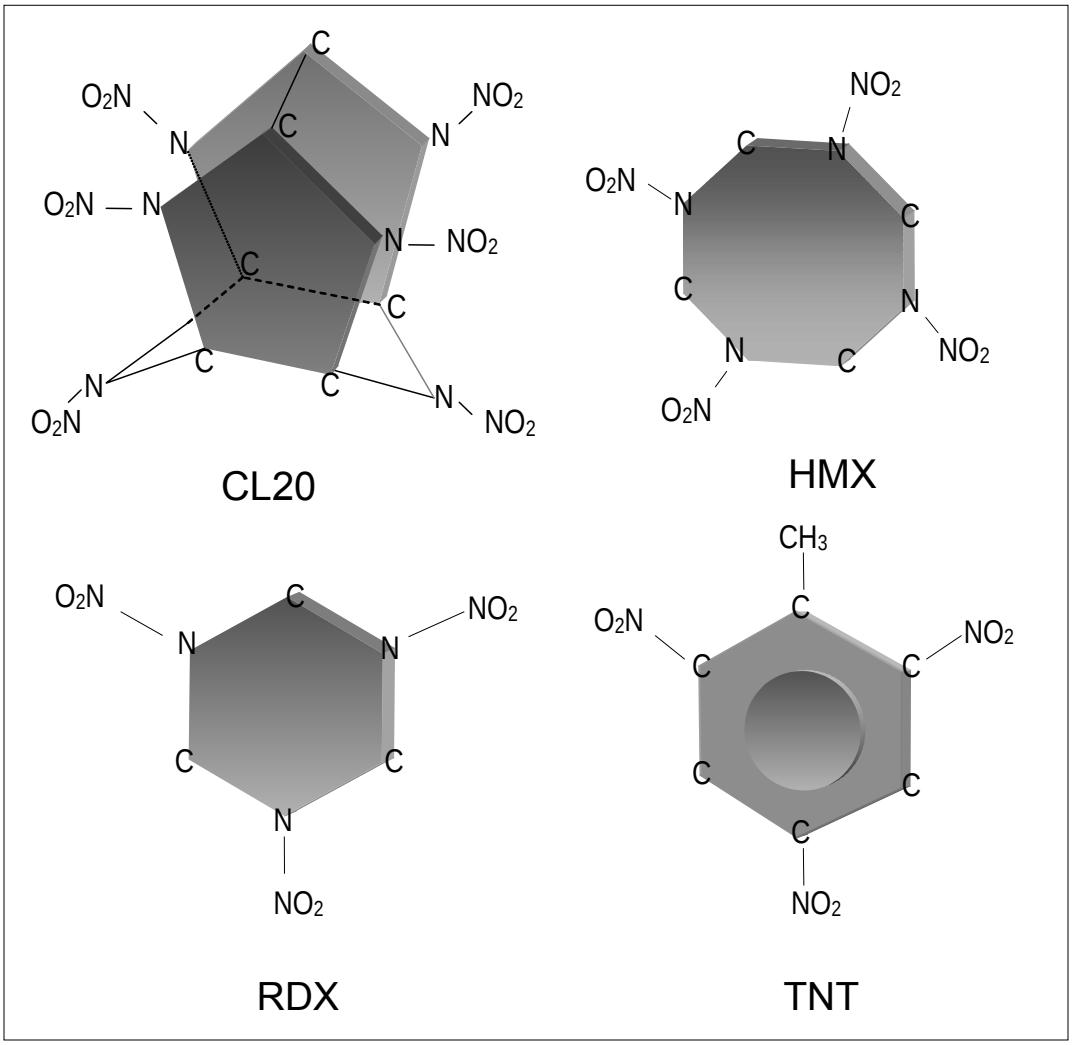

Figure 1. Structural formulas of selected energetic materials.

In this report, we describe a new ion probe that increases the SPF-FD technique's sensitivity by a factor of ten and we model the electric field of old and new probes in the presence of a substrate using an ion optics simulation program. We extend the SPF-FD technique to the detection of HMX, CL20, and TNT residues, determine their limits of detection (LOD) at ambient conditions, and present a more detailed study of the issues influencing sensitivity. We report the UV absorption spectrum of CL20 and measure its extinction coefficient at 248 nm.

2. Experimental Apparatus

Our previous publication contains the details of the SPF-FD technique (*14*). An abridged description of the experimental apparatus follows. Briefly, a 248-nm laser beam excites a thin film of energetic material placed on the surface of a quartz plate. We generate this beam by

doubling the output of a 10-Hz, Nd:YAG (neodymium:yttrium aluminum garnet)-pumped dye laser (Surelite III and Lambda Physik, FL3002) and direct it perpendicular to the substrate surface. We focus it with a 10-cm focal length quartz lens to a 2.9 x 10^{-3} cm^2 spot. A second laser beam, whose frequency is in the 224- to 226-nm range, ionizes the resulting NO photo-fragment by REMPI. We generate this laser beam by doubling the output of a 10-Hz, Nd:YAG-pump dye laser (Surelite II and Lumonics HyperEx 300) and direct it parallel to the substrate surface. We also focus this beam with a 10-cm quartz lens but to a 5- x 10^{-5}-cm^2 spot. The pump and probe laser energies are in the 10- to 20-μJ range. A pulse generator (Stanford Research Systems, DG 535) set at 1 ms controls the time delay between the lasers.

Figure 2 depicts two sets of miniature, stainless steel electrodes that collect the ions and electrons. The set shown in figure 2a (vertical electrodes) are perpendicular to the substrate surface and are approximately 15 mm by 15 mm in size with a 5-mm gap and are ~0.5 mm from the surface. A 700-V bias between them results in an average electric field of ~140 V/mm. The set in figure 2b (horizontal electrodes) are parallel to the substrate surface and are similar to the vertical electrodes, except that they have a 6-mm gap and contain 2-mm holes for the passage of the excitation laser beam. An 850-V bias between them yields an average field of ~140 V/mm, the same as in the vertical electrodes. The lower plate is insulated and is ~0.5 mm from the substrate surface. We mount each probe and substrate on an XYZ stage for precise, spatial alignment between excitation and probe laser beams. A current amplifier (Keithley 427, gain 10^6 to 10^7 voltage/amperage, time constant 0.01 ms) amplifies the electrode signal and a 125-MHz oscilloscope (Lecroy, 9400) monitors it. A personal computer records the signals from a "boxcar" averager (Stanford Research Systems, SR250).

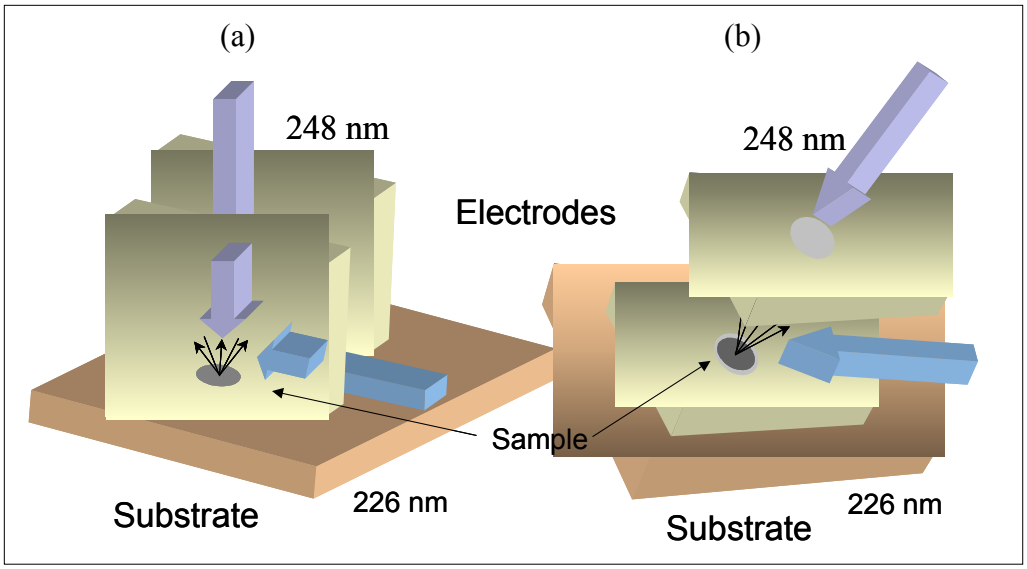

Figure 2. Ionization probes: (a) vertical electrodes whose electric field is parallel to the substrate surface; (b) horizontal electrodes whose electric field is normal to the substrate surface. (In a, the excitation laser beam is normal to the substrate, and the ionization laser is parallel to the substrate surface and 0.5 mm above it. In b, the excitation and probe beams are oriented as in a.)

We prepare thin films of RDX, HMX, CL20, and TNT by coating microscope slides with known volumes of diluted solutions of the target compound in acetone and then evaporating the solvent. For each LOD measurement, we use 4 to 10 slides with varying film thickness (surface concentration) of the selected explosive. We set the pump and probe lasers to 248 and 226.28 nm, respectively, and record the SPF-FD signal while moving the substrate so that each laser shot samples a fresh film spot. A plot of ion signal as a function of concentration yields the response plot for each compound. We record the SPF-FD spectra of the energetic materials by setting the excitation laser to 248 nm while scanning the ionization laser wavelength at a rate of 0.009 nm/s and simultaneously moving the substrate. Each spectrum is an average of three spectra.

Our colleagues at the U.S. Army Research Laboratory (ARL) provided us with the energetic materials. High pressure liquid chromatography (HPLC) analysis of the explosives reveals an HMX purity of more than 99.9% and an RDX, CL20, and TNT purities of more than 99%. A UV-visible spectrometer (Hewlett-Packard, Model 8453) with Hewlett-Packard Chemstation software records the absorbance spectra of 2.25×10^{-5} molar (M) RDX and CL20 in acetonitrile (HPLC-grade) in the wavelength region of 190 nm to 400 nm. The NO_2 (485 ppm in N_2) and NO (0.097% in argon) gases are from Matheson Tri-Gas and Airgas, respectively.

3. Results and Discussion

Figure 3 shows the SPF-FD spectra of RDX, HMX, CL20, and TNT films, along with a REMPI spectrum of diluted NO gas, in the region of 225.8 to 226.85 nm at 298 K and 1 atm via the horizontal ionization probe (figure 2b). We observe similar spectra with the vertical probe (figure 2a), but we do not observe any signal with either probe if the 248-nm laser is off or if there is no explosive on the substrate. The prominent spectral features of the explosives are similar to those of NO and are attributed to NO rotational lines of the Q_1+P_{21}, P_1, and P_2+Q_{12} branches of the A-X (0,0) band (*14*). The fact that the explosives yield a unique molecular fingerprint of NO is definitive proof that SPF-FD successfully detects residues of low vapor pressure explosives at ambient conditions. The overall SPF-FD mechanism involves the following steps:

$$\text{R-NO}_2\,(s) \xrightarrow{h\nu\ (248\ nm)} \text{R} + \text{NO}\,(X^2\Pi) + \text{O} \qquad (1)$$

$$\text{NO}\,(X^2\Pi) \xrightarrow{h\nu\ (226\ nm)} \text{NO}\,(A^2\Sigma^+) \xrightarrow{h\nu\ (226\ nm)} \text{NO+}\,(X^2\Sigma^+) + e\,, \qquad (2)$$

in which step (1) represents the laser excitation of a thin energetic film that yields ground state NO, and step (2) represents the (1+1) REMPI of the NO fragment by means of its real, intermediate $A^2\Sigma^+$ state ($\tau \sim 215$ ns). We observe an enhancement in the NO ionization because

the intermediate state's energy is resonant with one 226-nm photon. Steps (1) and (2) depict very efficient processes and require only a few micro-joules of laser radiation. The firing between the pump and probe lasers is set to 1 ms.

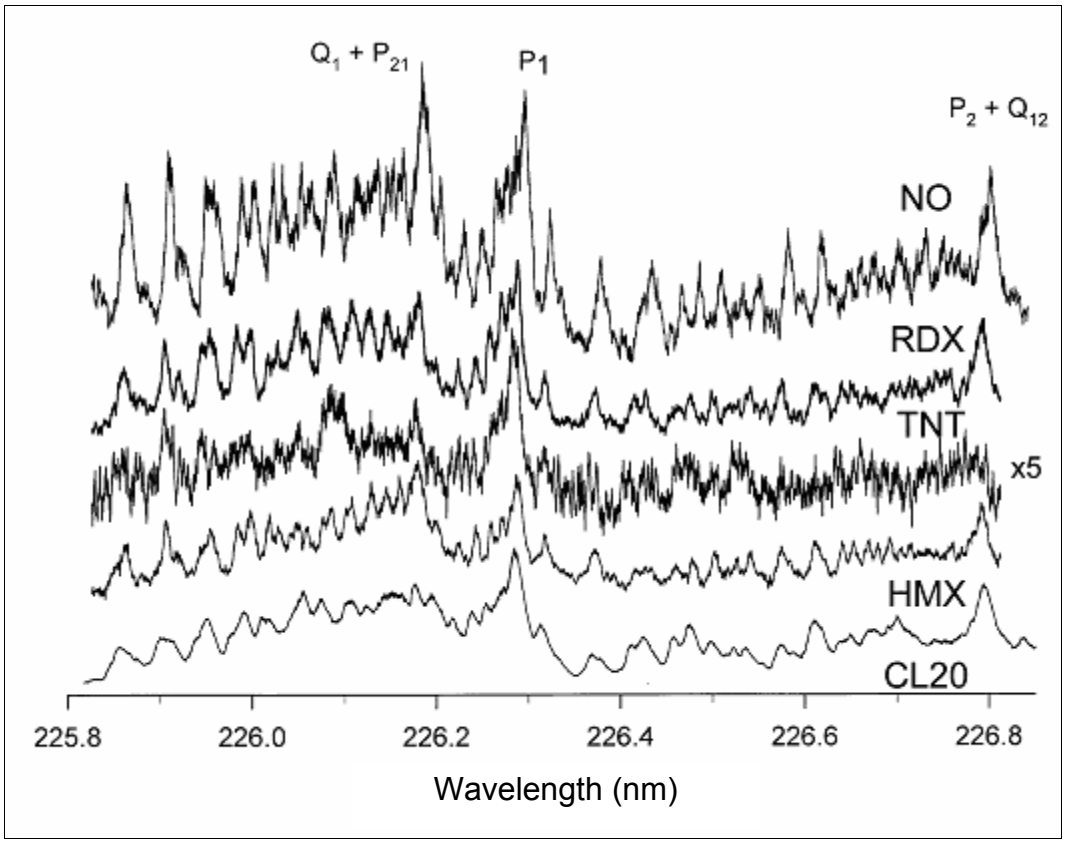

Figure 3. SLP-FD spectra of RDX, TNT, HMX, and CL20, and a REMPI spectrum of NO in the region of 225.8 to 226.8 nm. (The spectroscopic fingerprint of NO appears in the spectra of all the energetic materials.)

We determine the efficacy of both horizontal and vertical probes by testing them on RDX during identical operating conditions (same pump and probe laser energy and focal point size). Our results show that the horizontal probe with horizontal electrodes is about an order of magnitude more sensitive than the vertical probe with vertical electrodes. An important factor that contributes to the difference in sensitivity is the effect of the substrate on the probe's electric field. We investigate this effect with Simion 7.0, an ion optics design program (*15*).

Simion calculates the electric field and scalar potential between the electrodes in the presence of a substrate by solving the Poisson equation

$$\nabla^2 \phi = \frac{\rho}{\varepsilon},$$

in which ϕ is the electric potential, ε is the absolute permittivity, and ρ is the charge distribution. A "method of images" creates a valid solution of the electric potential by using the distribution of real charge plus "simulated" or "image" charge that is idealized to be on the other side of the plane defined by the substrate surface and that fulfills the boundary conditions. The potential for the point charge close to the substrate is a combination of the charge and its mirror "image" charge multiplied by a constant that is defined by

$$\frac{\kappa_e - 1}{\kappa_e + 1},$$

in which κ_e is the dielectric constant in the case of a linear isotropic homogeneous dielectric.

Figure 4 shows simulations of the vertical and horizontal probes' electric field with a dielectric substrate close to the probes. The top panels show some of the equipotential surfaces for the probes, whereas the bottom panels show a two-dimensional "slice" of the three-dimensional picture depicting the equipotential surfaces as equipotential lines. When the substrate is brought close to the edge of the vertical probe, a significant component of the electric field is oriented toward the substrate surface and away from the probe, as shown by the equipotential lines (the force vectors are normal to the equipotential lines and surfaces). The electrons or ions are forced away from the probe and are not collected. In contrast, the horizontal probe's electric field is mostly unperturbed as the substrate approaches the electrodes, as shown in the bottom of figure 2B, and all the charged species are collected. Thus, the horizontal probe is more sensitive than the horizontal probe. The horizontal probe also offers additional advantages over the vertical probe. First, it can sample metallic substrates because the high voltage electrode near the surface can be insulated, and second, it can be made to operate as a miniature ion mobility spectrometer for increased selectivity.

Our experiments on NO gas corroborate our simulation results on the two ion probes. Figure 5 shows the REMPI signal of 6 ppm NO in N_2 from the horizontal probe (trace A) and vertical probe (trace B) near a clean substrate. The flow rate of NO through the probes is ~5 l/min, the pump and probe lasers are set to 248 and 226.282 nm, respectively, and the probe beam is ~0.5 mm above the surface, as in the thin film experiments. Trace A has a 10-μs rise time and a decay with a shoulder. We attribute the signal to both photoelectrons (t ~ 0 to 20 μs) and positive ions (t >20 μs) generated from the ionization of NO. Although the probe is biased to collect the negative charges, the ions impact the opposite plate and generate an image charge on the collector plate, which manifests itself as a tail on the signal trace. The substrate does not perturb the probe's extraction field, and all the charged species are collected. Trace B also has a 10-μs rise time but an exponential decay. Its full width half maximum is ~20 μs. Trace B, unlike trace A, arises only from photoelectrons generated from the ionization of NO. The tail that results from the positive ions is absent, and the overall signal is reduced.

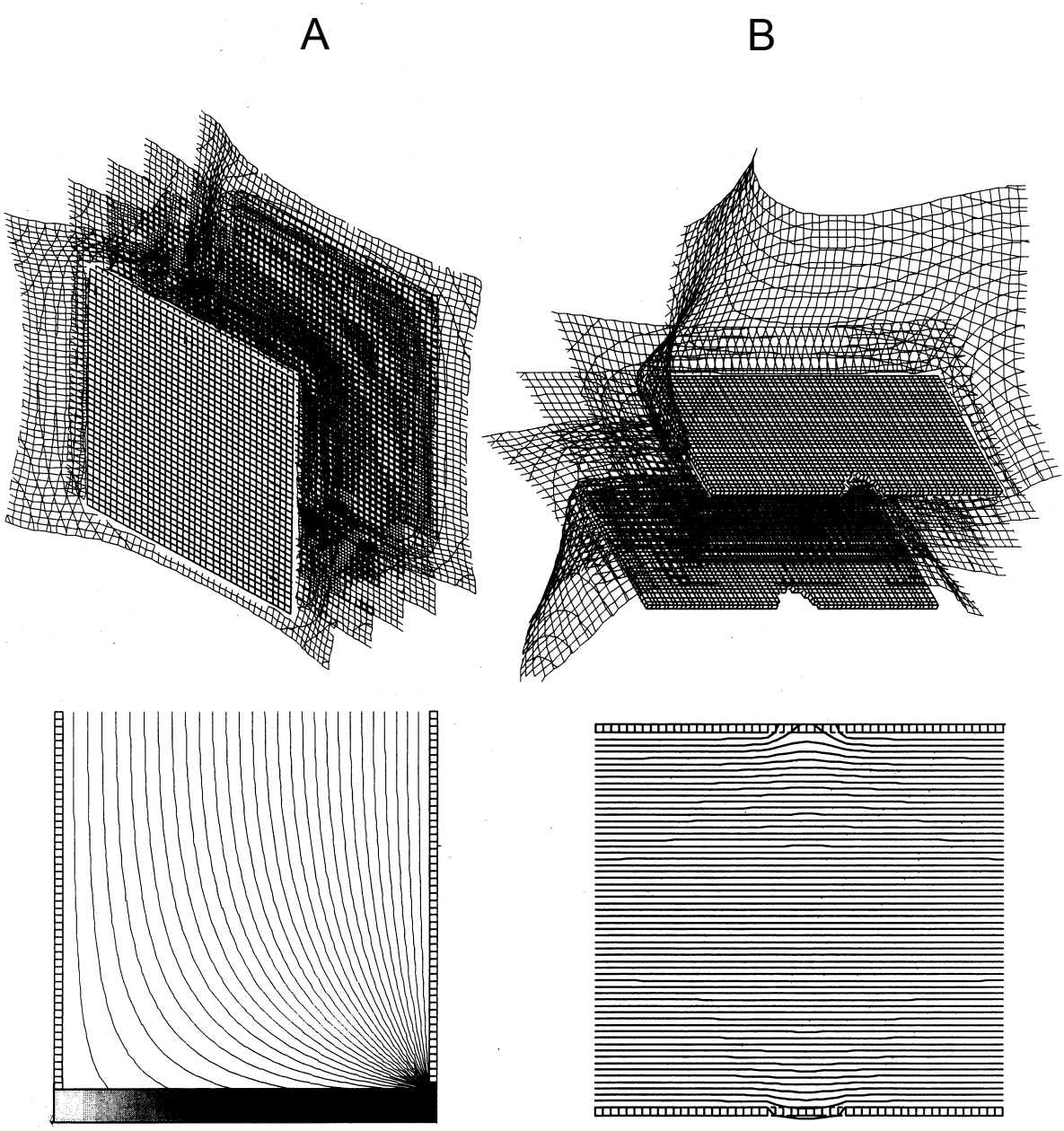

Figure 4. Simeon simulations of the electric field in the vertical and horizontal probes with the probes near a dielectric substrate. (Figure 4A shows a three-dimensional perspective of the vertical electrode's electric field [top panel] and a "slice" of the region between the plates showing the substrate and the equipotential lines within the plates [bottom panel]. Figure 4B shows the horizontal electrode's electric field with a perspective drawing in the top panel and a two-dimensional "slice" in the bottom panel. In the SPF-FD sampling region, the substrate disturbs the electric field in horizontal probe much less than in the vertical probe.)

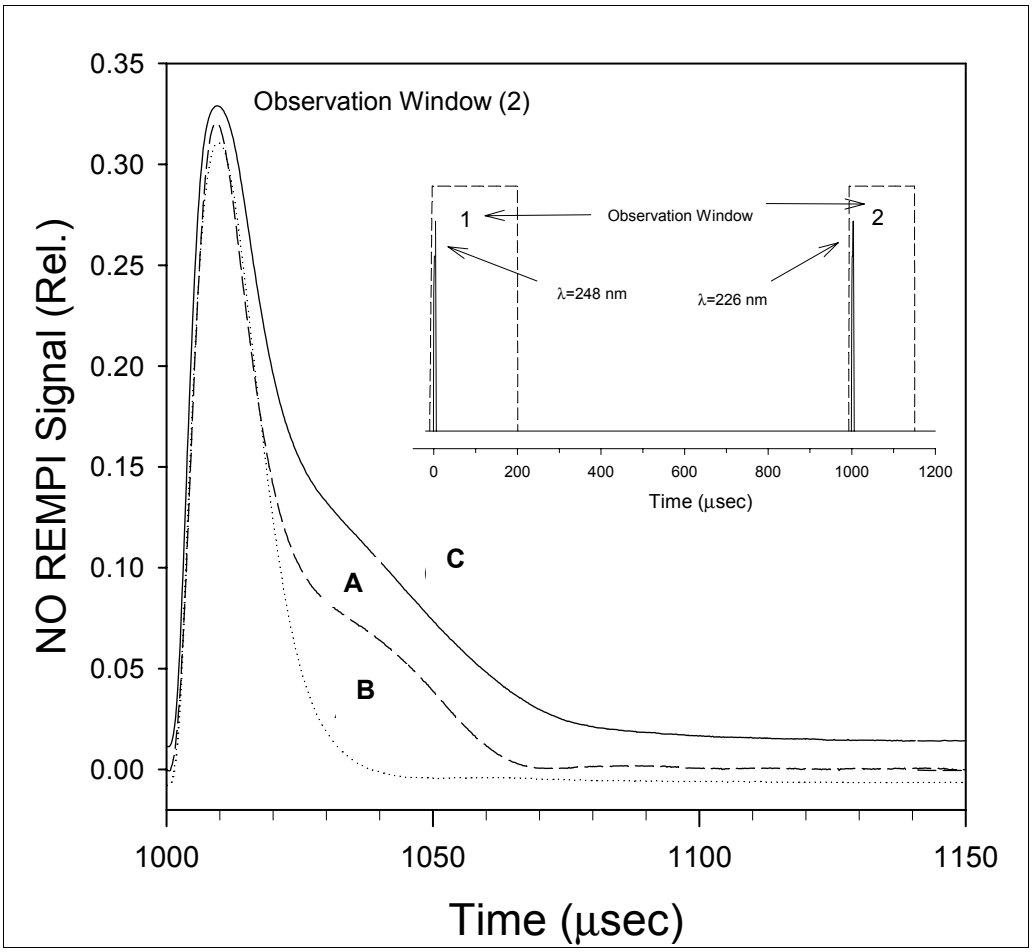

Figure 5. REMPI spectra at 226 nm of NO gas at ambient temperature and pressure. (The horizontal and vertical probes are near a clean substrate and the ionization laser is fired 1 ms after the excitation laser, as shown in the figure insert. The ionization laser beam passes through the center of the horizontal plates and near the edges of the vertical plates, slightly above the substrate's surface. Trace B from the vertical probe shows a weaker signal compared to trace A from the horizontal probe because the substrate perturbs the electric field in the vertical probe much more than in the horizontal probe. Trace C is from the vertical electrodes with the probe beam passing between plates at ~0.75 mm from the substrate surface [center of plates]. The vertical probe's electric field is nearly uniform because the substrate is not close to the ionization region and the resulting trace is similar to trace A.)

Figure 5, trace C, shows the REMPI signal of NO with the vertical probe near a clean substrate and the laser beam positioned between the electrodes at ~0.75 cm from the substrate (center of the electrodes). Positioning the probe beam at the electrode's center is ideal for detecting species in the gas phase because the field is uniform in this region and because the species concentration is the same as in the region close to the electrode's edge. Trace 5C is similar to trace 5A (horizontal probe) and results from the collection of photoelectrons and positive ions of NO. As expected, the signals are about the same, suggesting that both probes are equally effective in sampling species in the gas phase. However, the horizontal probe is more sensitive than the vertical probe

when one is sampling surface species because the beam in the vertical probe must be steered from the center of the electrodes (a region of relatively low concentration of surface species but uniform electric field) to the electrode's edge near the surface, where the species concentration is high but the electric field is perturbed by the substrate. The overall signal is thus reduced, and the sensitivity of the vertical electrodes for surface sampling is lower.

The probe's configuration and electric field orientation play a role in the extraction and collection of charged species from the 248-nm irradiation of the energetic films. Figure 6 shows both the vertical (trace A) and horizontal (trace B) probe signal from RDX at 248 nm with the 226-nm laser off. The 248-nm laser beam is normal to the vertical probe's electric field but parallel to the electric field of the horizontal probe. Both traces show the time evolution of the charged species. The curves have about the same area but different shapes. Most of the signal in trace A occurs in the first 50 μs, whereas the signal in trace B is distributed over 150 μs. We attribute the peaks to a combination of photoelectrons (t~15 μs) and molecular ions (t >15 μs). Although both probes collect the photoelectrons, the horizontal probe collects more of the ions. The origin and assignment of the positive ions are not well known and are the subject of future inquiry.

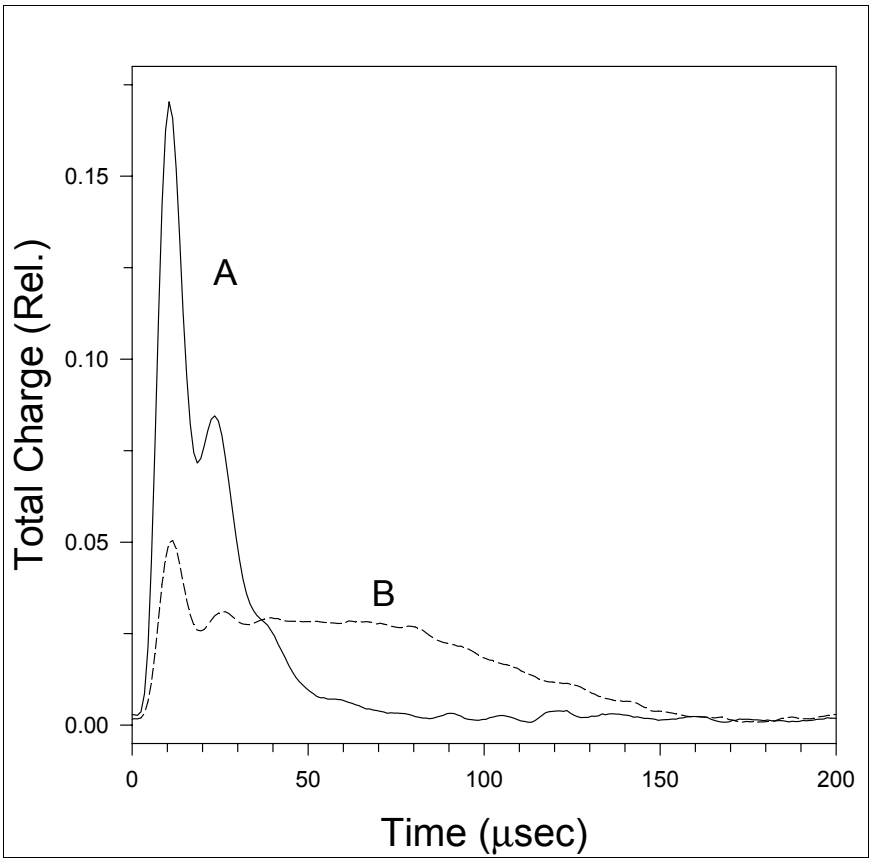

Figure 6. Total charge-time plot resulting from the prompt, 248-nm excitation of RDX with both the vertical probe (trace A) and horizontal probe (trace B). (The 226-nm probe laser is off.)

Figure 7 shows response curves of the various explosives at 248 and 226.28 nm for the pump and probe laser wavelength, respectively. The solid straight lines are best fits to the data, which are represented by symbols. The responses are directly proportional to the amount of material on the substrate for a fixed optical setup and laser energy. In all cases, the signal is observed over a wide range of concentrations. The LOD is defined by 3 σ/R, in which R is the response and σ is the root mean square of the noise. Table 1 shows the LOD for the various energetic materials. They are 1.4 ng/cm^2 for RDX, 2.0 ng/cm^2 for HMX, 7.1 ng/cm^2 for CL20, and 15.4 ng/cm^2 for TNT. Ranking the compounds by limit of detection yields a sensitivity of RDX > HMX > CL20 > TNT. The RDX value of 1.4 ng/cm^2 corresponds to sampling ~3.3 by 10^6 NO molecules (~0.4 fentogram [fg] of RDX) in the laser probe volume (*14*) and compares favorably to the 200-pg value obtained by Chang and coworkers (*16*). Table 1 shows that the LOD ratio of TNT to RDX is ~11. This value is similar to the value of 10 obtained by our group by one-laser PF-FD of gaseous RDX and TNT at 226 nm near ambient conditions (*6*). Probing the NO fragment by REMPI yielded TNT and RDX LODs of 70 and 7 ppb, respectively.

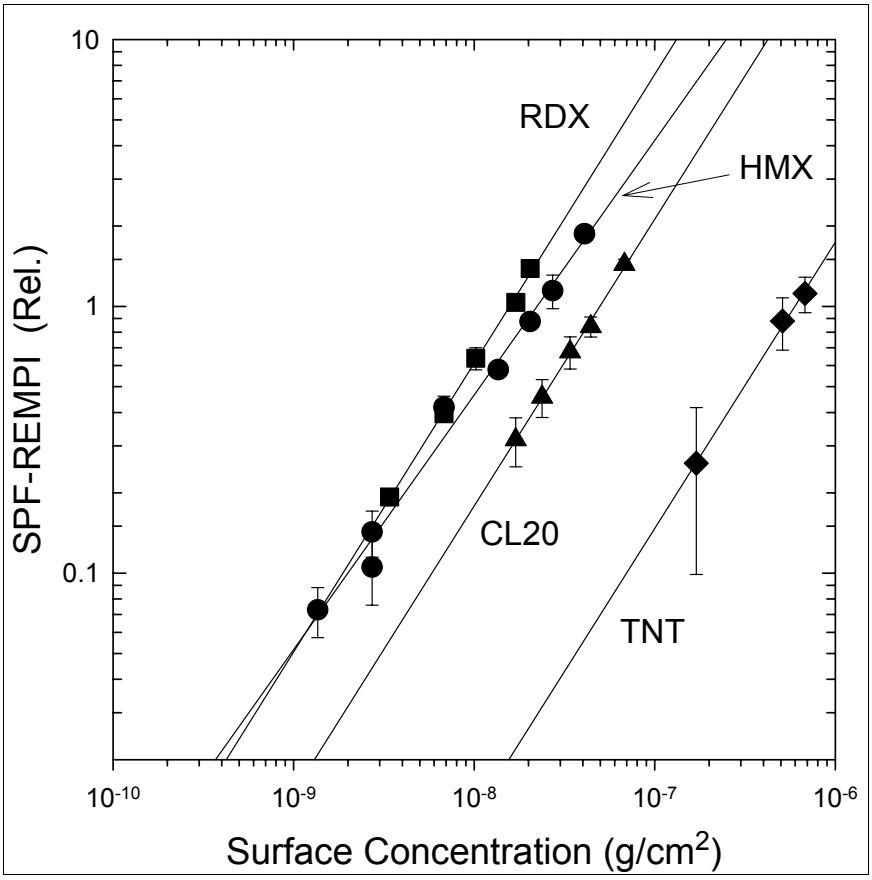

Figure 7. RDX, HMX, CL20, and TNT response plots with the horizontal probe. (The excitation and probe lasers are set at 248 and 226.28 nm, respectively.)

Table 1. Energetic materials with their limits of detection and extinction coefficients at 248 nm and their R-NO_2 bond dissociation energies.

Energetic Material	Limit of Detection at 248 nm (ng/cm^2)	Extinction Coefficient(s) at 248 nm (x10^3)	R-NO_2 Bond Dissociation Energy (kcal/mol)
RDX	1.4	7.6[b], 7.2[c], 6.8[d]	34.2[f], 34.3[g], 39.0[h]
HMX	2.0	9.4[d]	38.8[h]
CL20	7.1	15.0[b]	39.4[i]
TNT	15.4	13.6[d], 14.2[e]	>60[j]

a. $\varepsilon = \log (Io/I)/\ell c$, where Io is the intensity of the incident light, I is the intensity of the transmitted light, ℓ is path length in cm, and c is the concentration in moles/liter.
b. Present study, acitonitrile solvent.
c. Cabalo and Sausa, methanol solvent (*14*)
d. Scroeder and coworkers, ethanol solvent; an estimate from published spectra (*17*)
e. Kamlet and coworkers, methanol solvent; an estimate from published spectra (*18*)
f. Wu and Fried, calculation for gas-phase molecule (*19*}
g. Kuklja, calculation for molecule located near the surface of the crystal; the author reports a slightly higher value of 35.1 kcal/mole for a gas-phase molecule (*20*).
h. Chakraborty and coworkers; calculation for gas-phase molecule (*21*)
i. Rice, calculation for gas-phase molecule (*22*)
j. Gonzalez and coworkers (*23*)

The overall SPF-FD mechanism represented in steps (1) and (2) suggests that the LOD for each energetic material depends on the amount of NO produced at 248 nm, step (1), and the amount of NO detected at 226.28 nm, step (2). In our LOD measurements, the probe energy and optical setup are the same for all the compounds; thus, the amount of NO produced at 248 nm depends on the absorption coefficient of the target compound at 248 nm and the governing mechanism that produces NO. Figure 8 shows the ultraviolet absorption spectra of RDX and CL20 in the region of 200 to 320 nm. We are the first to report that of CL20. The 248-nm extinction coefficients for RDX and CL20 at 248 nm are 7.6×10^3 and 1.5×10^4, respectively, and are listed in table 1. Table 1 also shows the 248-nm extinction coefficient of RDX from our previous work, 7.2×10^3 (*14*), RDX, HMX and TNT values of 6.8×10^3, 9.4×10^3, and 13.6×10^3, at 248 nm, respectively, which we interpolate from extinction coefficient curves of Schroder and coworkers (*17*), and a TNT value of 14.2×10^3 at 248 nm, which we obtain from the work of Kamlet, Hoffsomer, and Adolph (*18*). All the RDX values, as well as the TNT values, are in good agreement, considering the different solvents used and the error in interpolation at 248 nm. Ordering the compounds by absorbance at 248 nm yields CL20 > TNT > HMX > RDX. *A priori*, we expect the compounds' LOD order to parallel their absorbance order. Surprisingly, this is not the case: the CL20 and TNT absorptivities are higher than those of RDX and HMX, yet their sensitivities are lower. Also, the absorptivity of CL20 is about the same as that of TNT, but its sensitivity is almost twice that of TNT. Clearly, the molecule's absorption coefficient at 248 nm plays less of a role in its LOD than the mechanism for generating NO.

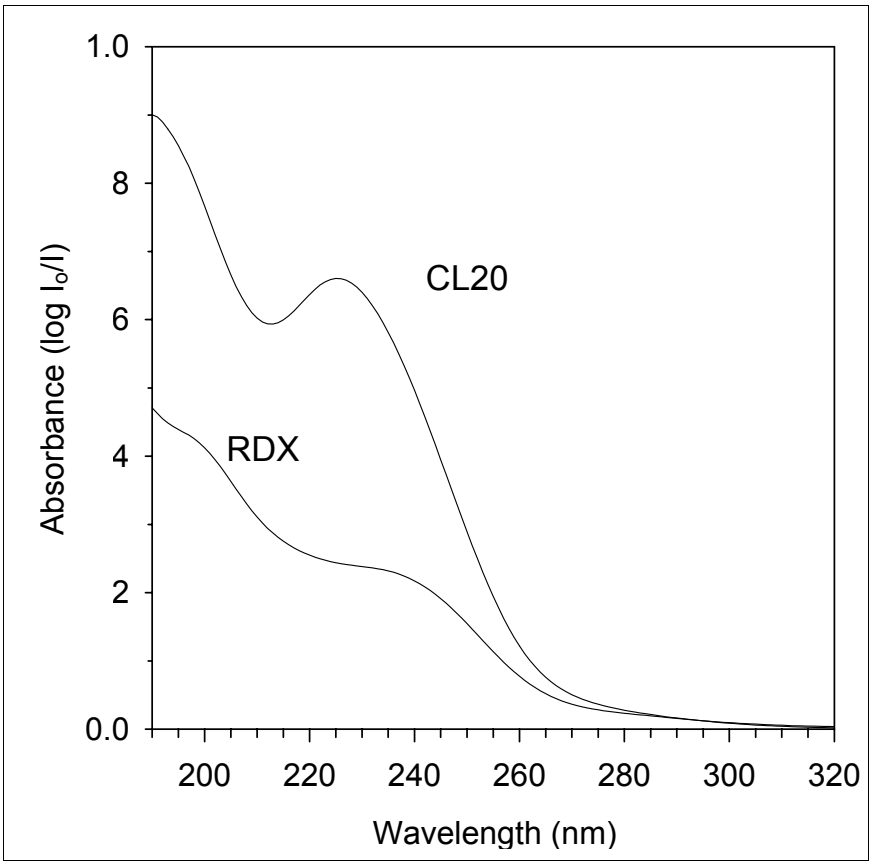

Figure 8. Absorbance curves of 2.25 x 10^{-5} M RDX and CL20 in acetonitrile in the 190- to 290-nm range.

The mechanisms involved in the 248-nm laser irradiation of RDX, CL20, HMX, and TNT on surfaces are complex. They may include photothermal and photochemical processes, as well as surface effects. Among the many suggested initial steps in the thermal decomposition of nitramines in the condensed phase, the most likely mechanism is the homolysis of the nitro-functional group, which is weakly attached to the remainder of the molecule. NO_2 may then react further to produce NO. Table 1 lists the R–NO_2 bond dissociation energy for the four compounds (*19* through *23*). Table 1 also shows that TNT has the highest bond dissociation energy for R–NO_2 scission by at least 20 kcal/mol. In part, this is because the NO_2 group in TNT is bonded to a carbon-atom-containing ring that is more stable than the nitrogen-atom-containing ring in the nitramines. Thus, TNT releases its NO_2 less readily than RDX, HMX, and CL20, and its LOD value is expected to be larger than the LOD of the nitramines. Also, TNT has several alternate decomposition pathways that compete with R-NO_2 bond scission. They include oxidation of –CH_3 to form anthranil (*21*), nitro/nitrite isomerization (*24*), and catalysis. These pathways also decrease the initial production of NO_2 and contribute to TNT's lower sensitivity relative to the nitramines.

The R-NO_2 bond dissociation energy of nitramines RDX, HMX, and CL20 is similar (around 34 to 39 kcal/mol). However, CL20 has an LOD that is a factor of nearly 3 times greater than the LOD of RDX and HMX. This suggests that the process of NO_2 release in these molecules is more complicated than the simple cleavage of a single nitro-functional group and may involve the loss of more than one nitro group from each molecule. In the case of RDX and HMX, the energy for the ring's C-N bond cleavage is lowered after the removal of the nitro-functional group, and further decomposition generating additional NO_2 is possible (*25*). In contrast, the C-N bond in CL20's backbone is stabilized following NO_2 homolysis, and further decomposition is hindered (*25, 26*). The backbone of RDX and HMX is two dimensional, and it is sterically difficult for the radical site to stabilize itself by interacting with its other parts. In the case of CL20, its cage structure promotes the stabilization of the radical site by rearrangement or multiple bond formation with other parts of the backbone and prevents additional NO_2 loss. Although our argument for CL20's LOD being larger than that of RDX and HMX is plausible, other governing processes may be operable.

Figure 9 shows an SPF-FD spectrum of NO from RDX with the horizontal probe, along with a spectral simulation of NO, in the region of 225.8 to 226.8 nm. Both spectra reveal NO rotational lines of the Q_1+P_{21}, P_1, and P_2+Q_{12} branches of the A-X (0,0) band. A multiparameter computer program based on a Boltzmann, rotational, distribution analysis generates the simulation spectrum. Parameters include laser line shape, rotational line strengths and energies, and temperature (*14*). The best fit of the data with a Gaussian function for the laser line shape yields a rotational temperature, T_R, of 304 ±10 K. This value agrees well with the value of 325 ±25 K that we obtain with the vertical probe (*14*) and indicates that the NO fragment is thermally equilibrated by collisions with O_2 and N_2 in the time scale of the experiment, as expected from gas kinetic calculations.

We also probe the NO fragment for vibrational excitation and determine its vibrational temperature. Laser radiation near 226 nm excites the NO A-X (0,0) transitions and probes the NO $X^2\Pi$ (v"=0) state, whereas laser radiation near 224 and 237 nm excites the (1,1) and (0,1) transitions, respectively, and probes the (v"=1) state. We observe significant signal from all the energetic materials at 226 nm but little, if any, at 224 nm or from RDX at 237 nm. This indicates that NO is formed primarily in its $X^2\Pi$ (v"=0) state with a vibrational temperature, T_v, of ~298K. The millisecond time of our experiment is sufficient to vibrationally relax NO, which requires a few microseconds. Heflinger and coworkers observe vibrationally excited NO $X^2\Pi$ (v"=2) from the 248-nm photolysis of TNT vapor near ambient conditions (*4*, *5*). This is not suprising because the time between the TNT photolysis and subsequent LIF detection of NO (~10 ns) is less than the time required for NO to vibrationally relax. Also, TNT experiences fewer collisions when it decomposes in the gas phase compared to the condensed phase.

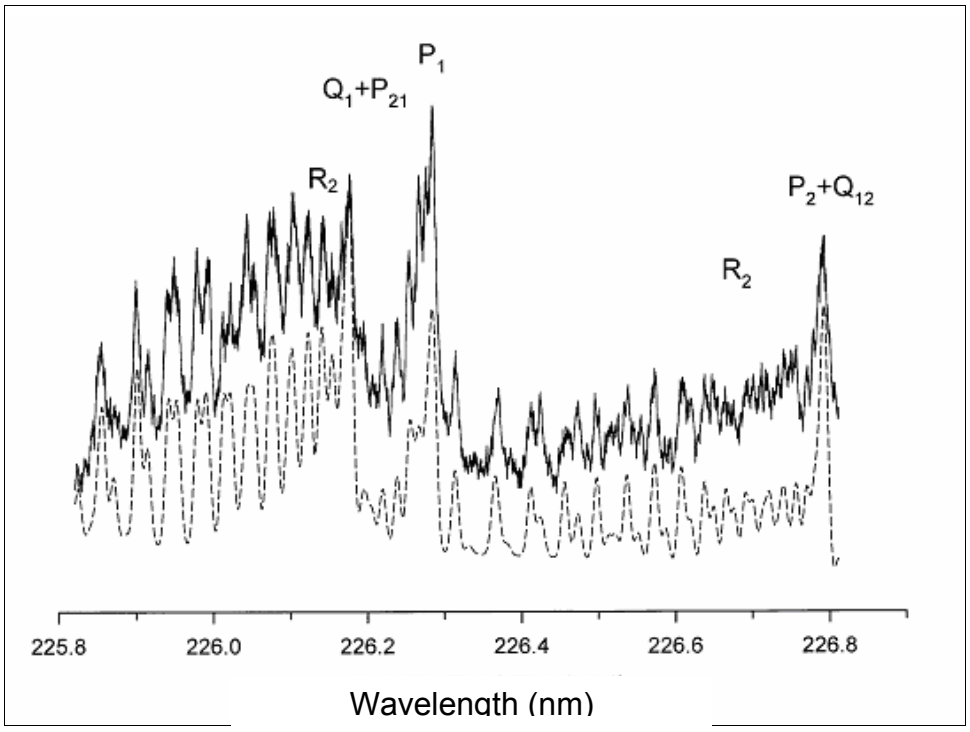

Figure 9. SPF-FD spectra of NO from RDX. (The dashed line is a best fit of the observed data, shown as a solid line. The spectra are offset for clarity. A Boltzmann analysis yields a rotational temperature of ~304 ±10 K.)

Unlike the 224-nm excitation of the energetic films, we observe a significant NO $X^2\Pi$ (v"=1) signal when we photolyze NO_2 gas at 224 nm. In this case, the time between the photolysis of NO_2 and ionization of NO (~6 ns) is insufficient to vibrationally thermalize NO. We do not observe any v"=1 signal from room temperature NO, as expected, because its Boltzmann, (v"=1/v"=0) ratio is $\sim 10^{-5}$ at 298 K. We calculate an NO_2 detection limit of ~150 ppb at 224 nm from this and previous work (*27*). This suggests that less than 150 ppb of NO_2 from the energetic film survives ~1 ms after the laser excitation pulse. Thus, the NO signal from the energetic films results probably from secondary reactions of NO_2 rather than the gas-phase photolysis of NO_2 emanating from the energetic film. Brill and coworkers show that NO_2 is the primary product from the rapid heating of CL20 (*25*) and RDX (*28, 29*), and along with HCN, by HMX (*28*). They observe that NO, if present at all in the early stages of the decomposition, increases rapidly as NO_2 reduces from secondary reactions. Geetha and coworkers corroborate these observations from their work on the thermal decomposition of CL20 (*6*).

4. Conclusions

We have demonstrated the analytical utility of SPF-FD spectroscopy for detecting trace concentrations of RDX, HMX, CL20, and TNT on surfaces with LODs in the low nanogram-per-square-centimeter range at atmospheric pressure and room temperature. A 248-nm laser excites the energetic film, and a second laser operating near 226 nm facilitates the detection of resulting NO fragment by REMPI. Both processes are efficient and require only a few microjoules of laser energy. The technique's sensitivity depends in part on the probe geometry, with the horizontal probe being a factor of ~10 more sensitive than the vertical probe. This is corroborated by our ion optics simulations, which reveal that substrate perturbs the electric field of the horizontal probe less than that of the vertical probe.

The sensitivity of the SPF-FD technique also depends on the photochemical and photothermal processes yielding NO. NO is rotationally and vibrationally equilibrated in the time scale of our experiment and is formed probably from secondary reaction of NO_2. TNT and CL20 have lower sensitivities than RDX and HMX, whose sensitivities are comparable. TNT's stronger R-NO_2 bond compared to that in the nitramines and decomposition pathways that compete with R-NO_2 homolysis might contribute to its low sensitivity. In the case of CL20, whose R-NO_2 bond strength is comparable to that of RDX and HMX, its cage structure probably inhibits the escape of additional NO_2 groups, after primary R-NO_2 homolysis, and may contribute to its low sensitivity.

In short, the SPF-FD approach with horizontal probe exhibits great potential for detecting trace energetic materials on surfaces in real time and *in situ* because of its high sensitivity and simplicity of instrumentation. Research on the photochemical and photothermal mechanisms involved in the ultraviolet irradiation of explosives residues is continuing.

5. References

1. Usachev, A.D.; Miller, T.S.; Singh, J.P.; Yueh, F.Y.; Jang, P.R.: Monts, D.L. Optical properties of gaseous 2,4,6-trinitrotoluene in the ultraviolet region. *Applied Spectroscopy* **2001**, *55*(2), 125–129.

2. Todd, M.; Provencal, R.; Owano, T.; Paldus, B.; Kachanov, A.: Volopyanov, K.; Hunter, M.; Coy, S.; Steinfeld, J.; Arnold, J. Application of mid-infrared cavity-ringdown spectroscopy to trace explosives vapor detection using a broadly tunable (6-8 μm) optical parametric oscillator. *Appl. Phys.* **2002**, *B 75*(2-3), 367–376.

3. Boudreaux, G.M.; Miller, T.S.; Kunefke, A.J.; Singh, J.P.; Yueh, F.; Monts, D. Development of a photofragmentation laser-induced-fluorescence laser sensor for detection of 2,4,6-trinitrotoluene in soil and groundwater. *Appl. Opt.* **1999**, *38*(9), 1411–1417.

4. Heflinger, D.; Arusi-Parpar, T.; Ron, Y.; Lavi, R. Application of a unique scheme for remote detection of explosives, *Optics Communications* **2002**, *204* (1-6), 327–331.

5. Arusi-Parpar, T.; Heflinger, D.; Lavi, R. Photodissociation followed by laser-induced fluorescence at atmospheric pressure and 24 degrees C: a unique scheme for remote detection of explosives. *Applied Optics* **2001**, *40* (36), 6677–6681.

6. Swayambunathan, V.; Singh, G.; Sausa, R. Laser photofragmentation-fragment detection and pyrolysis-laser-induced fluorescence studies on energetic materials. *Appl. Optics* **1999**, *38*(30), 6447–6454.

7. Swayambunathan, V.; Saysa, R.; Singh, G. Investigations into trace detection of nitrocompounds by one- and two-color laser photofragmentation/fragment detection spectrometry. *Appl. Spectrosc.* **2000**, *54*(5), 651–658.

8. Dionne, B.C.; Rounbehler, D.P.; Achter, E.K.; Hobbs, J.R.; Fine, D.H. Vapor pressure of explosives. *J. Energetic Mater.* **1986**, *4*, 447–47, and references therein.

9. Cundal, R.B.; Frank, T.F. Colin, C. Vapor pressure measurements of some organic high explosives *J. Chem. Society Faraday Transactions 1: Physical Chemistry in the Condensed Phases* **1978**, *74*(6), 1339–45.

10. Rosen, J.M.; Dickinson, C. Vapor Pressures and heats of sublimation of some high melting organic explosives. *J. Chem. Eng. Data* **1969**, *14* (1), 120–124.

11. References 8-10 report the vapor pressure of HMX, RDX, and TNT. The vapor pressure of CL20 is not reported in the open literature: it is probably much less than that of RDX at room temperature based on its molecular structure.

12. Tang, T.B.; Chaudhri, M.M.; Rees, C.S.; Mullock, S.J. Decomposition of solid explosives by laser irradiation-a mass-spectrometric study, *J. Mater. Sci*. **1987**, *22* (3), 1037–1044 (1987).

13. Dickinson, J.T.; Jensen, L.C.; Doering, D.L.; Lee, R. Mass-spectroscopy study of products from exposure of cyclotrimethylene-trinitramine single-crystals to KrF excimer laser-radiation. *J. Appl. Phys.* **1990** *67* (8), 3641–3651 (1990).

14. Cabalo, J.; R. Detection of hexahydro-1,3,5-trinitro-1,3,5-triazine (RDX) by laser surface photofragmentation-fragment detection spectroscopy. *Appl. Spectroscopy* **2003** , *57*(9), 1196–1199 (2003).

15. SIMION is an electrostatic lens analysis and design program developed originally by D. C. McGilvery at Latrobe University Bundoora Victoria, Australia, 1977. SIMION 7.0 is a PC-based program developed by David Dahl of the Idaho National Engineering and Environmental Laboratory. Additional information can be found at http://www.simion.com/.

16. Cheng, C.; Kirkbridge, T.E.; Batchelder, D.N. Lacey, R.J.; Sheldon, T.G. In-situ detection and identification of trace explosives by Raman Microscopy. *Journal of Forensic Sciences* **1995**, *40*, 31–37 (1995).

17. Schroeder, W.A.; Wilcox, P.E.; Trueblood, K.N.; Dekker, A.O. Ultraviolet and visible absorption spectra in ethyl alcohol: data for certain nitric esters, nitramines, nitroalkylbenzenes, and derivatives of phenol, aniline, urea, carbamic acid, diphenylamine, carbazole, and triphenylamine. *Analytical Chemistry* **1951**, *23*(12), 1740–1747.

18. Kamlet, M.J.; Hoffsommer, J.C.; Adolph, H.G. Steric Enhancement of Resonance. I. Absorption Spectra of the Alkyltrinitrobenzenes. *Journal of the American Chemical Society* **1962**, *84*(20), 3925–3828.

19. Wu, C.J.; Fried, L.E. Ab initio Study of RDX Decomposition Mechanisms. *J. Phys. Chem. A* **1997**, *101*, 8675–8679.

20. Kuklja, M.M.; Kunz, A.B. Electronic structure of molecular crystals containing edge dislocations. *Journal of Applied Physics* **2001**, *89* (9), 4962–4970.

21. Chakraborty, D.; Muller, R.P.; Dasgupta, S.; Goddard III, W.A. Mechanism for unimolecular decomposition of HMX (1,3,5,7-tetranitro-1,3,5,7-tetrazocine), an ab initio study. *J. Phys. Chem A* **2001**, *105*(8), 1302–1314.

22. Rice, B. of the US Army Research Laboratory, private communication. A preliminary density functional theory calculation at the B3LYP/6-31G* level yields a CL20 N-NO_2 bond strength of 38.6 kcal/mol. The error limit is ± a few kca/mol.

23. Gonzalez, A.C.; Larson, C.W.; McMillen, D.F.; Golden, D.M. Mechanism of decomposition of nitroaromatics- laser-powered homogeneous pyrolysis of substituted nitrobenzenes. *J. Phys. Chem.* **1985**, *89*(22), 4809–4814.

24. He, Y.Z.; Cui, J.P.; Mallard, W.G.; Tsng, W. Homogeneous gas-phase formation and destruction of anthranil from o-nitrotoluene decomposition. *J. Am. Chem. Soc.* **1988**, *110*(12), 3754–3759.

25. Patil, D.G.; Brill, T.B. Thermal decomposition of energetic materials 53. Kinetics and mechanisms of thermolysis of hexanitrohexazaisowurtzitane. *Combustion and Flame* **1991**, *87*, 145–151.

26. Geetha, M.; Nair, U.R.; Sarwade, D.B.; Gore, G.M.; Asthana, S.N.; Singh, H. Studies on CL20: the most powerful high energy material. *Journal of Thermal Analysis and Calorimetry* **2003**, *73*, 913–922.

27. Pastel, R.L.; Sausa, R.C. Spectral differentiation of trace concentrations of NO2 from NO by laser photofragmentation with fragment ionization at 226 and 452 nm: quantitative analysis of NO-NO2 mixtures. *Applied Optics* **2000**, *39*(15), 2487–2495.

28. Oyumi, Y.; Brill, T.B. Thermal-decomposition of energetic materials 3. A high-rate, in situ, FTIR study of the thermolysis of RDX and HMX with pressure and heating rate as variables. *Combustion and Flame* **1985**, *62* (3), 213–224.

29. Gongwer, P.E.; Brill, T.B. Thermal decomposition of energetic materials 73. The identity and temperature dependence of "minor" products from flash-heated RDX. *Combustion and Flame* **1998**, *115* (3), 417–423.

NO. OF COPIES ORGANIZATION

* ADMINISTRATOR
DEFENSE TECHNICAL INFO CTR
ATTN DTIC OCA
8725 JOHN J KINGMAN RD STE 0944
FT BELVOIR VA 22060-6218
*pdf file only

1 DIRECTOR
US ARMY RSCH LABORATORY
ATTN IMNE ALC IMS MAIL & REC MGMT
2800 POWDER MILL RD
ADELPHI MD 20783-1197

1 DIRECTOR
US ARMY RSCH LABORATORY
ATTN AMSRD ARL CI OK TL TECH LIB
2800 POWDER MILL RD
ADELPHI MD 20783-1197

1 COMMANDING GENERAL
US ARMY MATERIEL CMD
AMCRDA TF
5001 EISENHOWER AVE
ALEXANDRIA VA 22333-0001

1 INST FOR ADVNCD TCHNLGY
THE UNIV OF TEXAS AT AUSTIN
3925 W BRAKER LN STE 400
AUSTIN TX 78759-5316

1 US MILITARY ACADEMY
MATH SCIENCES CTR OF EXC
ATTN MDN MATH LTC RUGENSTEIN
THAYER HALL
WEST POINT NY 10996-1786

1 THE JOHNS HOPKINS UNIV
CPIA TW CHRISTIAN
10630 LTLE PTXT PKWY STE 202
COLUMBIA MD 21044-3200

1 OLIN ORDNANCE
V MCDONALD LIBRARY
PO BOX 222
ST MARKS FL 32355-0222

2 ARMY RESEARCH OFFICE
ATTN R SHAW D MANN
PO BOX 12211
RSCH TRIANGLE PARK NC 27709-2211

NO. OF COPIES ORGANIZATION

1 COMMANDER
US ARMY ARDEC
ATTN AMSTA AR WE D DOWNS
PICATINNY ARSENAL NJ 07806-5000

1 US NAVAL RESEARCH LAB
CHEMISTRY DIV CODE 6125
ATTN J RUSSELL
4555 OVERLOOK AVE SW
WAHINGTON DC 20375-5342

3 PA STATE UNIVERSITY
DEPT OF MCHNL ENGNRNG
ATTN S THYNELL T LITZINGER K KUO
UNIVERSITY PARK PA 16802

1 OKLAHOMA STATE UNIVERSITY
DEPT OF CHEMISTRY
ATTN D THOMPSON
STILLWATER OK 74078

1 UNIVERSITY OF TEXAS AUSTIN
DEPT OF AEROSPACE
ENG AND MECHANICS
ATTN P VARGHESE
AUSTIN TX 78712

1 CORNELL UNIVERSITY
DEPT OF CHEMISTRY
ATTN TA COOL
BAKER LABORATORY
ITHACA NY 14853

1 UNIVERSITY OF DELAWARE
ATTN T BRILL
CHEMISTRY DEPT
NEWARK DE 19711

1 UNIVERSITY OF FLORIDA
ATTN J WINFORDNER
DEPT OF CHEMISTRY
GAINSVILLE FL 32611

1 RENSSELAER PLYTCHNC INST
DEPT OF CHMCL BIO ENGNRNG
ATTN A FONTIJN
TROY NY 12181

1 DEPT OF THE ARMY
US ARMY RDECOM SOSI
ATTN TECHNOLOGY AFFAIRS OFC
6000 6TH STREET SUITE 100
FORT BELVOIR VA 22060

NO. OF
COPIES ORGANIZATION

ABERDEEN PROVING GROUND

1 DIRECTOR
US ARMY RSCH LABORATORY
ATTN AMSRD ARL CI OK (TECH LIB)
BLDG 4600

18 DIRECTOR
US ARMY RSCH LABORATORY
ATTN AMSRD ARLWM BD
W ANDERSON S BUNTE
C CHABALOWSKI
B FORCH B HOMAN
P KASTE A KOTLAR
K MCNESBY M MCQUAID
A MIZIOLEK J MORRIS
J NEWBERRY B RICE
R PESCE-RODRIGUEZ
R SAUSA J CABALO
A WILLIAMS S PIRIANO
BLDG 4600

10 DIRECTOR
US ARMY RSCH LABORATORY
ATTN AMSRD ARLWM BD R BEYER
A BIRK A BRANT T COFFEE
J COLBURN P CONROY
S HOWARD C LEVERITT
M NUSCA G REEVES
BLDG 390